SELF-SACRIFICIAL TEMPLATE SYNTHESIS OF FE-N-C CATALYSTS WITH DENSE ACTIVE SITES DEPOSITED ON A POROUS CARBON NETWORK FOR HIGH PERFORMANCE IN PEMFC

Li Jiao, Tanvir Alam Arman, Sooyeon Hwang, Javier Fonseca, Norbert Okolie, Ehab Shaaban, Gonghu Li, Ershuai Liu, Ugur Pasaogullari, Siddharth Komini Babu, et al.

SELF-SACRIFICIAL TEMPLATE SYNTHESIS OF FE-N-C CATALYSTS WITH DENSE ACTIVE SITES DEPOSITED ON A POROUS CARBON NETWORK FOR HIGH PERFORMANCE IN PEMFC

*Li Jiao[1,8], Tanvir Alam Arman [2], Sooyeon Hwang[3], Javier Fonseca[1], Norbert Okolie[4], Ehab Shaaban[4], Gonghu Li[4], Ershuai Liu[5], Ugur Pasaogullari[6], Siddharth Komini Babu[2], Sanjeev Mukerjee[5], Jacob Schatz Spendelow[2], David A. Cullen[*7], Frédéric Jaouen[*8], Qingying Jia[*5]*

[1]Department of Chemical Engineering, Northeastern University, Boston, Massachusetts, 02115, United States

[2] Material Physics and Application, Los Alamos National Laboratory, Los Alamos, 87545, United States

[3]Center for Functional Nanomaterials, Brookhaven National Laboratory, Upton, New York 11973, United States

[4]Department of Chemistry, University of New Hampshire, Durham, New Hampshire, 03857, United States

[5]Department of Chemistry and Chemical Biology, Northeastern University, Boston, Massachusetts, 02115, United States

[6]Department of Mechanical Engineering, University of Connecticut, Connecticut, 06269, United States

[7]Center for Nanophase Materials Sciences, Oak Ridge National Laboratory, Oak Ridge, Tennessee 37831, United States

[8]ICGM, Univ. Montpellier, CNRS, ENSCM, Montpellier, 34293, France

Abstract:

Iron-nitrogen-carbon (Fe-N-C) single-atom catalysts are promising sustainable alternatives to the costly and scarce platinum (Pt) to catalyze the oxygen reduction reactions (ORR) at the cathode of proton exchange membrane fuel cells (PEMFCs). However, Fe-N-C cathodes for PEMFC are made thicker than Pt/C ones, in order to compensate for the lower intrinsic ORR activity and site density of Fe-N-C materials. The thick electrodes are bound with mass transport issues that limit their performance at high current densities, especially in H_2/air PEMFCs. Practical Fe-N-C electrodes must combine high intrinsic ORR activity, high site density and fast mass transport. Herein, we have achieved an improved combination of these properties with a Fe-N-C catalyst prepared via a two-step synthesis approach, constructing first a porous Zn-N-C substrate, followed by transmetallating Zn by Fe via chemical vapor deposition. A cathode comprising this Fe-N-C catalyst has exhibited a maximum power density of 0.53 W cm^{-2} in H_2/air PEMFC at 80 °C. The improved power density is associated with the hierarchical porosity of the Zn-N-C substrate of this work, which has been achieved by epitaxial growth of ZIF-8 onto g-C_3N_4, leading to a micro-mesoporous substrate.

Keywords: proton exchange membrane fuel cells, oxygen reduction reaction, Fe-N-C, chemical vapour deposition

1 Introduction

Hydrogen-fed proton exchange membrane fuel cells (PEMFCs) convert chemical energy into electrical energy with very low or zero-emission, making it a promising decarbonized technology for transportation applications and portable devices. One of the major challenges for the widespread deployment of PEMFCs is to disengage from its current dependence on costly and scarce platinum (Pt).[1] It is thus appealing to develop sustainable alternatives made of inexpensive and earth-abundant materials to catalyze the reaction requiring by far the highest Pt loading in PEMFCs, namely the oxygen reduction reaction (ORR). The state-of-the-art alternatives are catalysts with atomically dispersed nitrogen-coordinated iron sites (FeN_4) covalently integrated into porous carbon matrices (denoted as Fe-N-C).[2-4] Fe-N-C catalysts have demonstrated encouraging initial ORR activity approaching that of Pt/C in H_2/O_2 PEMFCs.[5-6] However, the performance of Fe-N-C cathodes in H_2/air PEMFCs is much lower than that of Pt-based ones under the same conditions, especially at high current density regimes, due to low accessibility of FeN_4 sites. This is, in turn, a combination of general intrinsic properties of Fe-N-C materials (high microporosity, low gravimetric active site density) and thicker cathodes as necessary to reach a sufficient number of active sites per geometric area of the MEA.[7] Besides durability issues of Fe-N-C materials, this power performance gap in H_2/air PEMFCs between Pt/C and Fe-N-C cathode has hampered the replacement of Pt-based catalysts by Fe-N-C catalysts.

The state-of-the-art Fe-N-C catalysts present high performance at elevated potentials such as 0.9 V in H_2/O_2 PEM fuel cells (all potentials in this work are given versus a reversible hydrogen electrode). This has been achieved by utilizing high catalyst loading in the range of 4-7 $mg_{Fe\text{-}N\text{-}C}$ cm^{-2} to increase the number of active sites per geometric area of the electrode, so as to compensate for the relatively low turnover frequency (TOF) and low gravimetric site density of FeN_4 active sites in comparison with those of Pt-based active sites in Pt/C materials.[6, 8-9] However, such high Fe-N-C loadings result in thick electrodes (> 100 μm), slow transport of oxygen and water, as well as low proton conduction through the catalytic layer. The effect can be particularly deleterious to the performance with H_2/air PEMFCs due to

the dilution of O_2 with N_2 at the cathode.[10] Consequently, the power densities achieved by Fe-N-C cathodes at the desired PEMFC operating voltage (0.6-0.7 V) are usually low, making them impractical. To alleviate these issues, Fe-N-C catalysts with various morphologies and porosities have been designed using hard silica templates or washable salt templates as well as polymers as soft templates.[11-17] The main goal of these syntheses was to create hierarchical porous structures combining micro, meso, and/or macroporosity in order to facilitate mass transport. However, these syntheses involved complicated template fabrication and harsh template removal procedures.[18-19] It is therefore tempting to create hierarchical porous carbon structures for Fe-N-C catalysts without a template removal process. Typical template-free approaches to preparing Fe-N-C catalysts generally start by finely mixing carbon, nitrogen, and iron precursors followed by heat treatment. The convoluted thermal–development of iron, nitrogen, and carbon species during pyrolysis results however in a low degree of freedom to simultaneously control active site density, catalyst's morphology and pore size distribution.[2] The conditions of the thermal treatment (atmosphere, duration, temperature, etc.) affect the nature and number of the formed single-atom FeN_4 sites, that have been widely acknowledged to be responsible for the superior ORR activity of Fe-N-C catalysts.[2, 4, 20-21] Meanwhile, the morphology, structure, and chemistry of the carbon matrix of the Fe-N-C catalysts also depend on the conditions of the thermal treatment. With such an approach where both the carbon matrix and Fe-based sites are formed simultaneously in the first pyrolysis step, it is therefore difficult to simultaneously optimize the site density and the catalyst morphology. It would be appealing to develop a multi-step synthetic approach that deconvolutes the step at which the active site density is defined from the step at which the catalyst's morphology is defined. In our previous study, Fe-N-C catalysts with abundant and gas-accessible FeN_4 sites were prepared by chemical vapor deposition (CVD).[6] The FeN_4 sites formed via high-temperature transmetalation between gaseous $FeCl_3$ and ZnN_4 moieties from a Zn-N-C substrate are naturally accessible to the gas phase in the resulting Fe-N-C materials. In addition, the morphology of the carbon matrix of the Zn-N-C substrate had no observable changes during the CVD process.

The CVD method thus potentially allows for sequentially and independently achieving a Zn-N-C substrate with optimum porous structure and high density of FeN_4 sites. Based on this concept, we designed a novel Zn-N-C substrate with a multimodal pore size distribution by growing zeolitic imidazolate frameworks-8 (ZIF-8) nanocrystals on graphitic carbon nitride (g-C_3N_4) nanosheets. ZIF-8-on-g-C_3N_4 epitaxial heterostructure benefits the creation of a porous carbon matrix to facilitate mass transport through the resulting Fe-N-C catalyst layer. A cathode comprising this Fe-N-C catalyst has exhibited a maximum power density of 0.53 W cm^{-2} in H_2/air PEMFC at 80 °C.

2 Results and Discussion

Our design principle is to construct a highly porous Zn-N-C substrate with high gas and water permeability, which can potentially not only form a high density of FeN_4 sites later via iron CVD but also possess excellent mass transport features. Based on this principle, ZIF-8 nanocrystals were directly grown on graphitic carbon nitride to mitigate their aggregation during thermal pyrolysis so as to create and expose more surface area of Zn-N-C substrate during CVD.

The synthesis procedure is illustrated in **Figure 1a** while the details are provided in the experimental section. First, the bulk solids of graphitic carbon nitride (g-C_3N_4) were synthesized by calcination of melamine at 550 °C. To facilitate the crystal growth of ZIF-8 nanocrystals on g-C_3N_4 nanosheets, the latter was first ball milled and exfoliated by sonication to nanosheets in methanol containing 2-methylimidazole. Then, a solution of $Zn(NO_3)\bullet 6H_2O$ in methanol was added under stirring. After that, the suspension was collected and washed with fresh methanol before being dried in an oven. Figures (1b), (1c) and (1d) show that the polyhedron ZIF-8 nanocrystals were grown on the g-C_3N_4 nanosheets. X-ray diffraction (XRD) patterns suggest that the ZIF-8 nanocrystal structure was obtained (Figure 1e). The composite ZIF-8/g-C_3N_4 precursor was then pyrolyzed in flowing argon at 1050 °C to produce a substrate (labeled as Zn-N-C_g). The latter was then converted to an iron-based catalyst (labeled as Fe-N-C_g) with the iron CVD method recently reported by us for the first time.[6] The porosity of the Zn-N-C_g substrate

was evaluated by N_2 adsorption/desorption. Types I and IV isotherms (Figure 1f) indicate the co-existence of micropores and mesopores.[22-23] In addition, the high gas uptake at the higher relative pressure ($P/P_0 > 0.9$) suggests the presence of abundant macropores. Specifically, the micropore diameter is centered at 1.78 nm with a total micropore volume of 0.6 $cm^3 \cdot g^{-1}$. The dominant mesopore diameter is around 4.0 nm with a total mesopore volume of 0.7 $cm^3 \cdot g^{-1}$ (Figure 1g). The total surface area of Zn-N-C_g is 944 $m^2 \cdot g^{-1}$, higher than that of the substrate (807 $m^2 g^{-1}$) synthesized in the absence of g-C_3N_4 (labelled as Zn-N-C in Figure 1g).[6] Thus, the introduction of g-C_3N_4 improves the porosity of the substrate, especially promoting the formation of mesopores (Figure 1g).

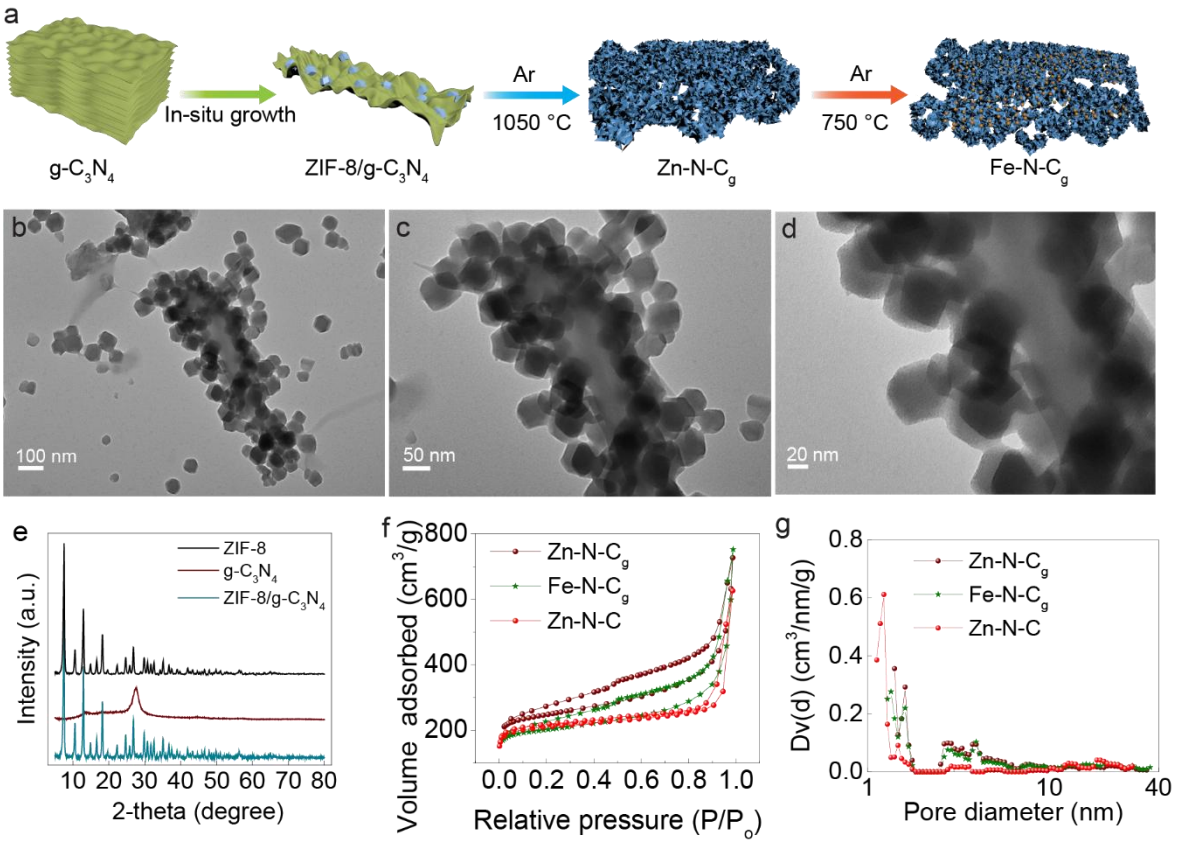

Figure 1. (a) Schematic illustration of the synthesis procedure. **(b)**, (**c**), and **(d)** representative TEM images of ZIF-8/g-C_3N_4 precursor at different magnifications. (**e**) XRD patterns of the ZIF-8/g-C_3N_4 precursor, ZIF-8, and g-C_3N_4 reference. (**f**) N_2 sorption isotherm curves. (**g**) pore size distribution calculated by applying the Non-Local Density Functional method. Zn-N-C data is from our previous report, with Zn-N-C synthesized in the same conditions as Zn-N-C_g but without g-C_3N_4.[6]

The morphology of the Zn-N-C_g substrate was further observed by high-resolution microscopy. **Figures 2a** and 2b show the scanning electron microscopy (SEM) images. As seen, a representative Zn-N-C_g particle has a three-dimensional interconnected network with abundant pores throughout. The morphology differs strikingly from the carbonaceous material derived from pyrolyzed ZIF-8 nanocrystals in the absence of g-C_3N_4, or with the post-addition of g-C_3N_4. In those cases, the carbonaceous materials have polyhedral-like nanoparticles.[6, 24] We attribute the difference, mainly, to the epitaxial heterostructure of the composite ZIF-8/g-C_3N_4 precursor.

Given the essential roles of Zn and nitrogen species in the formation of FeN_4 sites, Z-contrast dark-field scanning transmission electron microscopy (STEM) images were recorded for the Zn-N-C_g substrate. High-intensity Zn sites are visible all over the three-dimensional frameworks of Zn-N-C_g particles (Figure 2c-g). The energy-dispersive X-ray spectroscopy (EDS) mapping independently indicates Zn and N sites are uniformly dispersed within the Zn-N-C_g substrate (Figure 2e-g). Atomic-resolution aberration-corrected annular dark-field scanning transmission electron microscope (ADF- STEM) images further demonstrate the atomic dispersion of Zn atoms in the Zn-N-C_g substrate (Figure 2h and 2i). Each Zn atom is primarily surrounded by four nitrogen atoms (noted as ZnN_4 structure), as indicated by the fit of the Fourier Transform of the extended X-ray absorption fine structure (FT-EXAFS) spectrum at the Zn K-edge (Figure 2j). The presence of a small FT-EXAFS peak around 2 Å (without phase correction) (Figure 2j) suggests the existence of low contents of metallic zinc, in addition to the Zn-N_4 moieties.

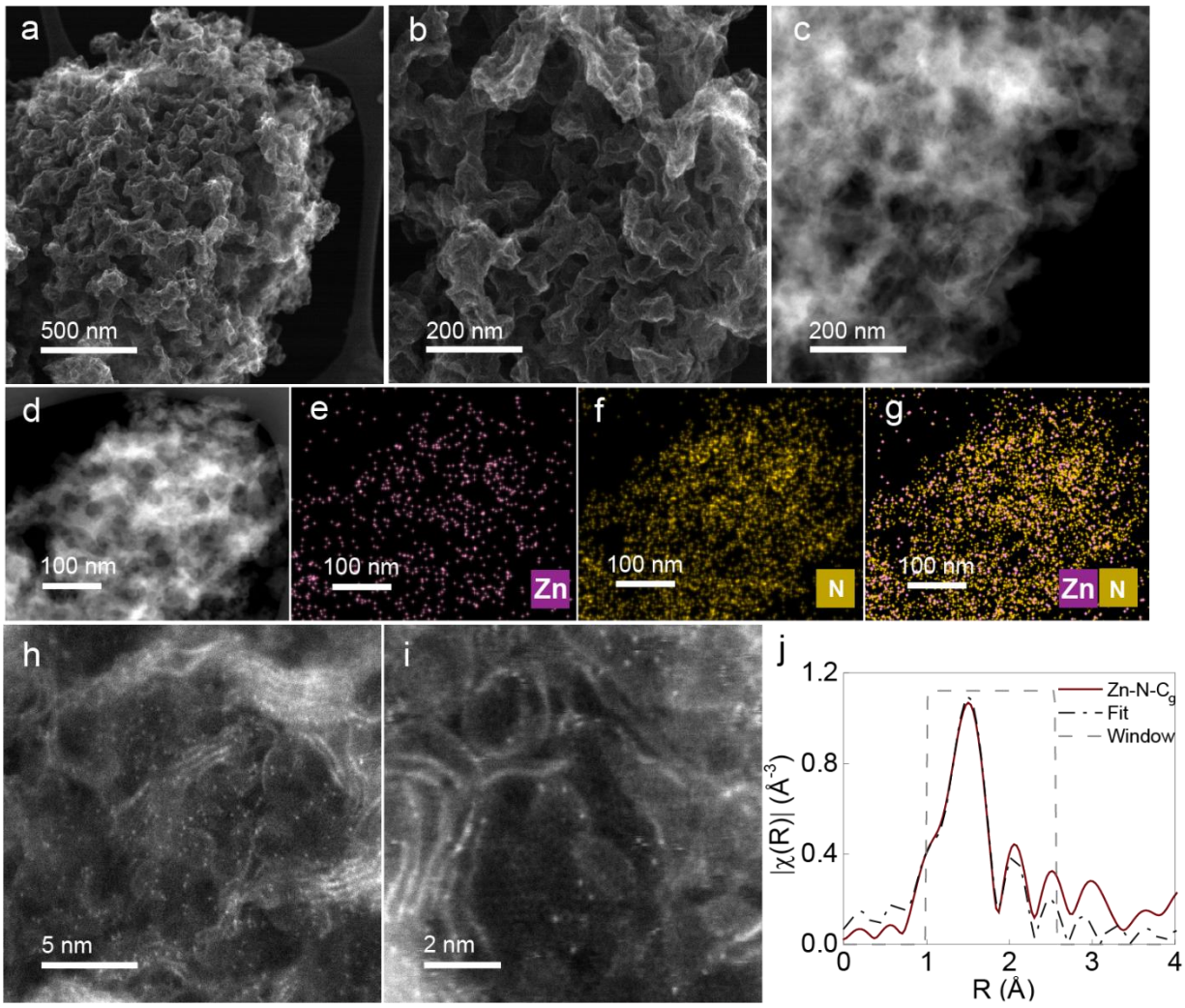

Figure 2. Characterization of Zn-N-C_g. (**a**) and (**b**) SEM images at different magnifications. (**c**)-(**g**) Z-contrast STEM images and energy-dispersive X-ray spectroscopy (EDS) elemental distribution maps of zinc (**e**), nitrogen (**f**), and their overlapping image (**g**). (**h**) and (**i**) aberration-corrected annular dark-field (ADF) STEM images. (**j**) ex situ Zn K-edge Fourier-transformed EXAFS spectrum and its fitting. R is interatomic distance. The indicated radial distance is not corrected for phase shift. χ(R) is the Fourier transform in the R space.

The ORR activity of the Fe-N-C_g catalyst was first evaluated in 0.5 M H_2SO_4 using a rotating disc electrode (RDE). A 0.85 V half-wave potential ($E_{1/2}$) was demonstrated, coupled with a well-defined diffusion-limited current density of 4.2 mA·cm^{-2}~~, close to the expected value for 4-e ORR at 900 rpm~~ (**Figure 3a**). Compared with Zn-N-C_g, the substantial increase in ORR activity highlights the essential role of iron in the superior ORR activity of the Fe-N-C catalyst in acid media. The Tafel plot derived from

the ORR polarization curve shows a kinetic current density of 16 $mA \cdot cm^{-2}$ (20 mA per milligram catalyst) at 0.8 V. This activity compares favorably with the state-of-the-art Fe-N-C catalysts.[25]

To evaluate the potential application in PEMFCs, the Fe-N-C_g catalyst was integrated into the membrane electrode assembly (MEA) by blade coating an ink comprising the catalyst and Nafion D521 ionomer on a Nafion 211 membrane (noted as MEA_{blade_Nafion} where Nafion in the superscript stands for the ionomer used in the cathode ink). At 80 °C and 100 % relative humidity (RH), the Fe-N-C_g cathode showed much higher H_2/air performance in the low potential region than achieved previously by us for the same synthesis but without g-C_3N_4 (noted as FeNC-CVD-750 catalyst) (Figure 3b). Specifically, the maximum power density of Fe-N-C_g is 0.49 $W \cdot cm^{-2}$ in those conditions, higher than 0.37 $W \cdot cm^{-2}$ for the FeNC-CVD-750 catalyst. Given that the cell performance of both catalysts is comparable at high potential (similar ORR kinetics), the superior performance of Fe-N-C_g in the low potential region in H_2/air PEMFCs strongly suggests that the introduction of g-C_3N_4 successfully improved the mass transport properties in H_2/air PEM fuel cells.

To explore the potential application of Fe-N-C_g catalyst at low RH, the MEA_{blade_Nafion} was also measured at 50 and 75% RH at a cell temperature of 80 °C. At high potentials (> 0.7 V), the current density was ca. 0.2 A cm^{-2} and independent of the RH (Figure 3c). Even at low potential (high current density), the cell performance decreased only slightly with decreasing RH. For example, the current density at 0.5 V decreased only from 0.95 A cm^{-2} at 100% RH to 0.86 A cm^{-2} at 75% RH and to 0.7 A cm^{-2} at 50% RH. This is correlated with increasing high-frequency resistance and cathode sheet resistance with decreased RH (Figure S2), assigned to proton resistance through the PEM and through the cathode layer, respectively. For comparison, a commercial Fe-N-C catalyst (~600 $m^2 \cdot g^{-1}$) synthesized with a silica template resulted in a much stronger decrease in performance with decreasing RH: the current density at 0.5 V decreased from ~0.32 A cm^{-2} at 100% RH to ~0.17 A cm^{-2} at 75% RH when the ionomer content was 35 wt%.[26-27] Similarly, carbon-supported (Ketjenblack) Pt nanoparticles also showed a strong

decrease in performance with decreasing RH. For example, the current density at 0.5 V decreased from ~1.9 A cm^{-2} at 100% RH to ~1.5 A cm^{-2} at 55% RH.[28] The decrease was attributed to low proton conductivity limiting the utilization of active sites, especially those located in narrow and long pores.[29-30] It was also reported that at low RH and similar Pt loading as well as the same I/C ratio, the Ketjenblack-supported Pt catalyst electrode had higher proton resistance and tortuosity than that of Vulcan XC-72 supported Pt catalyst.[31-32] Thus, we hypothesize that the exceptionally low dependence of performance on RH in the range of 100-50 % observed here for the Fe-N-C_g cathode is due to the high accessibility of FeN_4 sites and a short average path between FeN_4 sites and the ionomeric phase.

To explore the oxygen diffusion property of the Fe-N-C_g cathode layer, air was replaced by helox (He: 79%, O_2: 21%). As oxygen diffuses around four times more readily through helium than through nitrogen ($D_{O2\text{-}N2}$ = 0.74 ~1.13 × 10^{-4} m^2/s against $D_{O2\text{-}He}$ = 0.18 ~0.28 × 10^{-4} m^2/s at 25 °C and 1 atmospheric pressure), [33-34] the switch from air to helox at the cathode can lead to improved cell performance if strong limitation by O_2 gas-phase diffusion takes place in the pores of the cathode active layer.[35-36] As shown in Figure 3c, the ORR performance at 80 °C and 100 % RH was slightly lower in H_2/helox than that in H_2/air. Electrochemical impedance spectroscopy measurements were carried out at 0.5 A·cm^{-2} and showed identical high-frequency resistance (Figure S1). This result rules out that the slightly lower cell performance with helox stems from a different cell resistance. We can thus conclude from the helox test that O_2 gas-phase diffusion is not or negligibly limiting the H_2/air cell performance. The small decay in performance from air to helox is attributed to the slight decrease of Fe-N-C_g cathode ORR activity during the H_2/air test preceding the helox test carried out on the same MEA.

Next, we turned our attention to the choice and effect of ionomer inside the cathode layer. It was reported that high ion exchange capacity (low equivalent weight, EW) ionomers lead to a higher proton conductivity and water uptake, subsequently yielding a lower proton resistance and local oxygen transport resistance in the electrode layer.[37-40] Inspired by these reports, the long-side chain Nafion D521 ionomer (Nafion, EW 1100 g/mol) was replaced by the short-side chain Aquivion ionomer (Aquivion, EW 720

g/mol) in the Fe-N-C_g ink, keeping all other parameters the same. The resulting MEA is noted as $MEA_{blade\_Aquivion}$. The $MEA_{blade\_Aquivion}$ was measured at the same H_2/air conditions as the MEA_{blade_Nafion} at 80 °C and 100 % RH. As shown in Figure 3d, the $MEA_{blade\_Aquivion}$ shows a moderately improved performance at all potentials, reaching a maximum power density of 531 mW·$cm^{-2.}$ The constant upshift of the polarization curve for $MEA_{blade\_Aquivion}$ vs. MEA_{blade_Nafion} of ~ 30 mV indicates that the improvement is mainly related to the improvement in ORR kinetics, not due to an improvement in the proton conductivity throughout the cathode layer, which would otherwise lead to a current dependency of the improvement. It is also consistent with the EIS results showing that the presence of the lower EW Aquivion ionomer in the electrodes of the $MEA_{blade\_Aquivion}$ did not significantly affect the cathode sheet resistance (Figure S3).

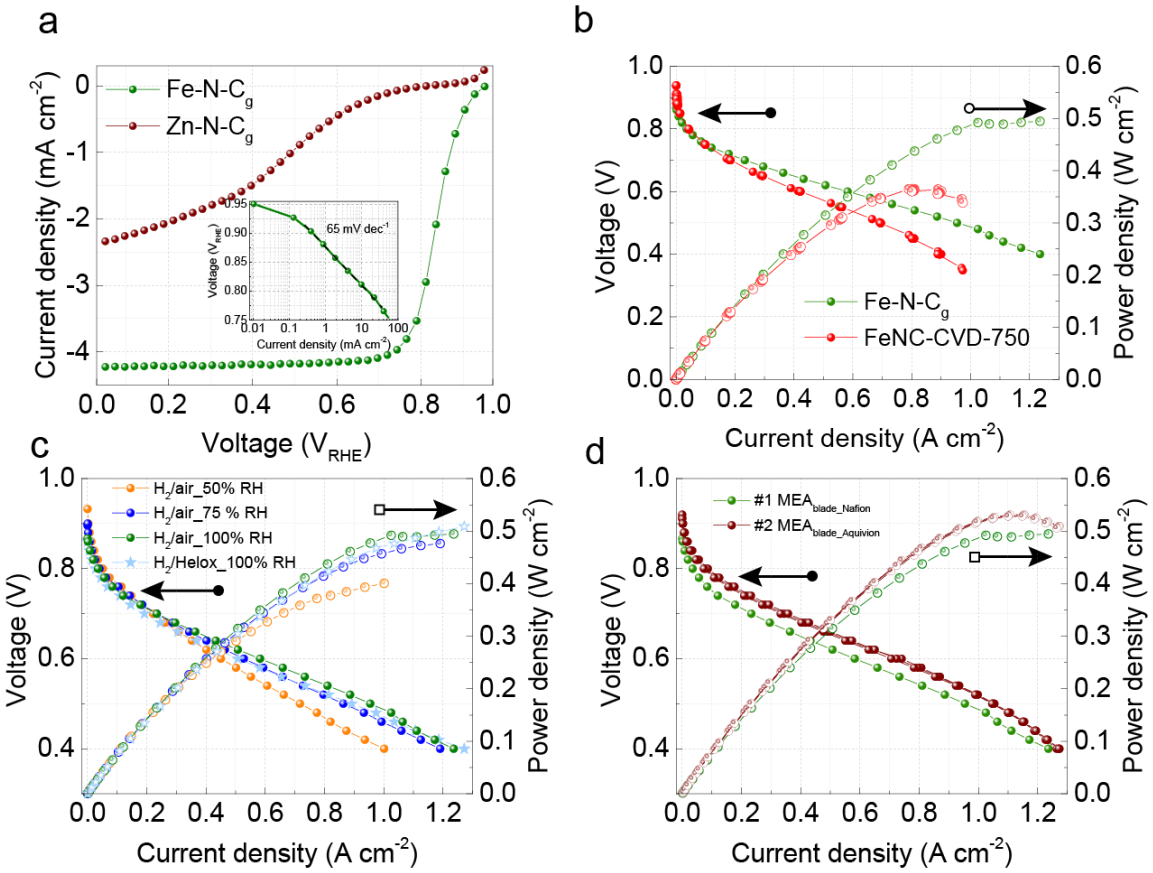

Figure 3. Electrochemical characterization of Fe-N-C_g catalyst. (**a**) Steady-state rotating disc electrode (RDE) polarization curves in O_2-saturated 0.5 M H_2SO_4 at room temperature, 900 r.p.m., 0.8 mg cm^{-2}

catalyst loading. Inset: Tafel plot derived from ORR polarization curve of Fe-N-C_g catalyst. (**b)-(c)-(d).** Beginning of life PEMFC polarization curves. (**b**) Comparison between Fe-N-C_g and FeNC-CVD-750 cathodes. Fe-N-C_g cathode electrode of MEA_{blade_Nafion}: 5.8 mg cm^{-2}, 100 % RH and 80 °C, H_2: 0.5 L/min, air 2.0 L/min, 150 kPa absolute at anode and cathode. FeNC-CVD-750 cathode: 6.0 mg cm^{-2}, 100 % RH and 80 °C, H_2: 0.5 L/min, air: 2.0 L/min, 150 kPa. Reproduced with permission. [6] Copyright 2021, under exclusive license to Springer Nature Limited. (**c**) Effect of RH and cathode feed on the initial performance for Fe-N-C_g cathode of MEA_{blade_Nafion}: cathode loading 5.8 mg cm^{-2}, 80 °C, H_2: 0.5 L/min, air or helox: 2.0 L/min, 150 kPa absolute at anode and cathode. (**d**) Initial performance for Fe-N-C_g of $MEA_{blade\_Aquivion}$: cathode loading 5.8 mg cm^{-2}, 100 % RH and 80 °C, H_2: 0.5 L/min, air: 2.0 L/min, 150 kPa absolute at anode and cathode.

The stability of the Fe-N-C_g cathode electrode (assembled into a fresh MEA, noted as MEA_{spray_Nafion}) was evaluated with an accelerated stress test involving repeatedly cycling the PEMFC voltage between 0.9 V and 0.6 V in H_2/air, at 80 °C and 100 % RH (**Figure 4a**). The initial polarization curve and polarization curves after different numbers of voltage cycles between 0.6 V to 0.9 V (from 1 to 30,000 cycles) were collected under the same experimental conditions. The current density at 0.8 V dropped from 0.1 A cm^{-2} initially to 0.045 A cm^{-2} after 1,000 voltage cycles and further decreased to 0.024 A cm^{-2} after 5,000 voltage cycles and 0.015 A cm^{-2} after 10,000 voltage cycles. Changes in the surface chemistry were also investigated by recording cyclic voltammograms of the cathode in the H_2/N_2 cell configuration (Figure 4b). The intensity of the redox peak at 0.8 V gradually diminished with increasing cycling number, while the capacitance did not change significantly (Figure 4b). This suggests that carbon oxidation did not significantly occur (which would lead to the surge of pseudocapacitance due to oxygen functional groups and possibly also increased capacitance due to increased carbon area), but the active site density decreased. While the origin of the redox peak in Fe-N-C catalysts is complex[41], experimental evidence provided by in situ X-ray absorption spectroscopy supports its assignment to Fe(II)/Fe(III) redox transition of FeN_4 sites, for some catalysts at least [3, 21] We therefore relate the presence of the redox peaks to the presence of electrochemically active FeN_4 sites in the Fe-N-C_g catalyst. Correspondingly, the disappearance of the redox peaks after 30, 000 cycles is ascribed to demetallation during the voltage cycling. This assignment is further supported by the result that the prominent redox peaks are present in the CV of the Fe-N-C_g catalyst but absent in the CV of the counterpart Zn-N-C_g (Figure S4). Based on these results we derived that demetallation is one primary reason for the degradation of the Fe-N-C_g

electrode in H_2/air PEMFCs. The poor stability of the Fe-N-C catalysts made by CVD observed here and also previously[6] can be reasoned by CVD maximizing surface exposure of FeN_4 sites and the exclusive presence of poorly stable D1 sites found by Mössbauer spectroscopy for the FeNC-CVD-750 catalyst.

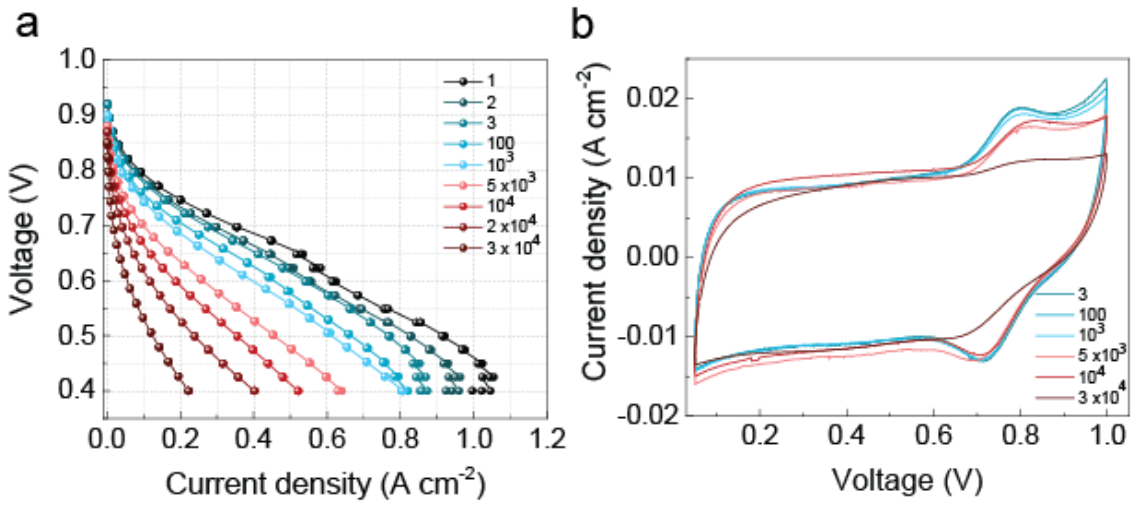

Figure 4. Stability measurement of the Fe-N-C_g catalyst. (a) PEMFC polarization curves for Fe-N-C_g catalyst at initial (labeled as 1) and after different voltage cycling (from 2 to 3 ×10^4 cycles) labeled as 2, 3…3 ×10^4) from 0.9 V to 0.6 V. 5.0 mg cm^{-2}, 100 % RH and 80 °C, H_2: 0.5 L/min, air: 1.0 L/min. 150 kPa absolute at both anode and cathode, **(b)** CV curves at 20 mV/s with H_2 and N_2 flow in the anode and cathode, respectively.

To understand the source of its exceptional ORR performance in H_2/air PEMFCs, the Fe-N-C_g catalyst was characterized by multiple techniques. The Fe-N-C_g catalyst inherited the porous three-dimensional network features of the Zn-N-C_g substrate (**Figure 5a**, 5b, and 5c). Compared with the Zn-N-C_g substrate, The Fe-N-C_g catalyst has a slightly lower microporous volume (0.5 cm^3/g vs 0.6 cm^3/g for Zn-N-C_g) and a slightly higher mesoporous volume (0.88 cm^3/g vs 0.7 cm^3/g for Zn-N-C_g) (Figure 1f and 1g). The Z-contrast dark-field STEM images show iron atoms as bright dots throughout the carbon matrix without visible aggregation (Figures 5d and 5e). Energy-dispersive X-ray spectroscopy (EDX) mapping (Figures 5f, 5g, 5h, and 5i) also signifies that iron and nitrogen sites were uniformly dispersed. To further identify the iron distribution, atomic-level STEM images were performed (Figure 5j). Plenty of bright dots were observed, for which the electron energy-loss spectroscopy spectrum shows the proximity of single iron

and nitrogen atoms (Figure 5k). This suggests the presence of abundant FeN_x moieties in the Fe-N-C_g catalyst. The Fe K-edge X-ray absorption near-edge structure (XANES) spectrum of the Fe-N-C_g catalyst (Figure 5l) overlaps that of the $Fe^{III}Pc$-O_2 reference compound, which suggests that the average oxidation state of iron in the Fe-N-C_g is close to +3. This precludes the presence of large amounts of metallic Fe^0 species, further supported by the absence of prominent FT-EXAFS peaks at ca 2.2 Å, characteristic of the Fe-Fe interaction from metallic species (Figure 5m). The absence of FT-EXAFS signal at 2.5-2.7 angstrom also excludes the presence of significant amounts of ordered ferric oxides, and the iron, therefore, seems to be present as $Fe^{III}N_x$ sites, in line with the iron speciation found in FeNC-CVD-750 catalyst prepared similarly but in absence of g-C_3N_4.[6] The fitting of the FT-EXAFS spectrum implies the dominant iron sites are O_2-FeN_4, indicating that the FeN_4 moieties are mostly gas-accessible. These results in combination demonstrate that a porous three-dimensional network with abundant gas-accessible FeN_4 sites was achieved on the Fe-N-C_g catalyst.

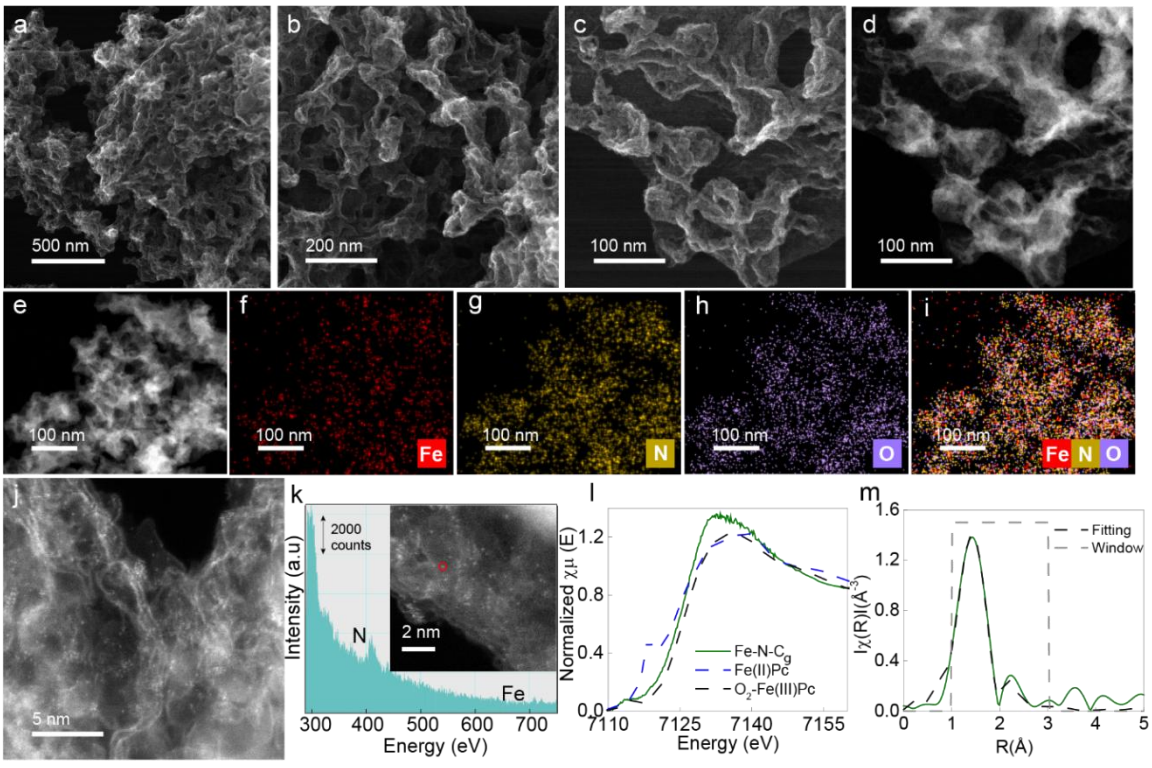

Figure 5. Characterization of Fe-N-C_g catalyst. (a), (b) and (**c**) SEM images at different magnifications. (**d**)-(**i**) Z-contrast STEM images and EDS elemental distribution maps of iron (**f**), nitrogen (**g**), oxygen (**h**),

and their overlapping image (**i**). (**j**) aberration-corrected ADF-STEM images. (**k**) electron energy-loss spectroscopy showing the N K edge and Fe L edge acquired from a single atom (the bright dot in the inset in which an atomic-resolution AC-STEM image is displayed). (**l**) ex situ XANES spectrum together with those of Fe (II)Pc and O_2-Fe(III)Pc reference compounds for comparison. (**m**) ex situ Fe K-edge Fourier-transformed EXAFS spectrum and the fitting. R is interatomic distance. The indicated radial distance is not corrected for phase shift. χ(R) is the Fourier transform in the R space.

To understand the high activity of the Fe-N-C_g catalyst, we quantified its electrochemically active site density by nitrite stripping. This protocol involves the reaction of nitrite anions with FeN_x moieties to form the stable nitrosyl adduct and its subsequent electrochemical reduction in a lower potential region. The associated stripping charge allows for quantifying the number of active sites.[42-43] After exposure of Fe-N-C_g electrode to a NO_2^- the solution, the ORR activity was significantly decreased (**Figure 6a**), evidencing NO_2^- poisoned the active sites in the Fe-N-C_g catalyst. Subsequently, the NO_2^- reductive stripping in the lower potential region was conducted. The associated stripping area (the grey area in Figure 6b) was integrated to calculate the stripping charge. After stripping, the ORR performance was mostly recovered (Figure 6a). Note that the hypothesis on the number of electrons transferred (three or five electrons) during the reduction of one nitrosyl adduct, which is required to calculate the site density, is currently under debate.[43-44] Assuming three electrons transfer during nitrite stripping with hydroxylamine as reduction product[44], the site density of Fe-N-C_g is around 0.8×10^{20} sites per gram of the catalyst, slightly lower than that (1.92×10^{20}) of our previous FeNC-CVD-750 catalyst. On the other hand, assuming five electrons transfer with NH_4^+ as the reduction product, the site density of Fe-N-C_g is around 4.8×10^{19} sites per gram of the catalyst. Even under this assumption, this value compares favorably to the reported 0.25 ~1.44×10^{19} sites per gram of several benchmark Fe-N-C catalysts, derived from nitrite stripping and assuming five electrons reduction.[6, 26] The maximum power density of the Fe-N-C_g catalyst (0.53 W cm^{-2}) is higher than that of the FeNC-CVD-750 catalyst (0.37 W cm^{-2}) (Figure 3b) owing to improved mass transport of the Fe-N-C_g electrode, albeit the lower site density.

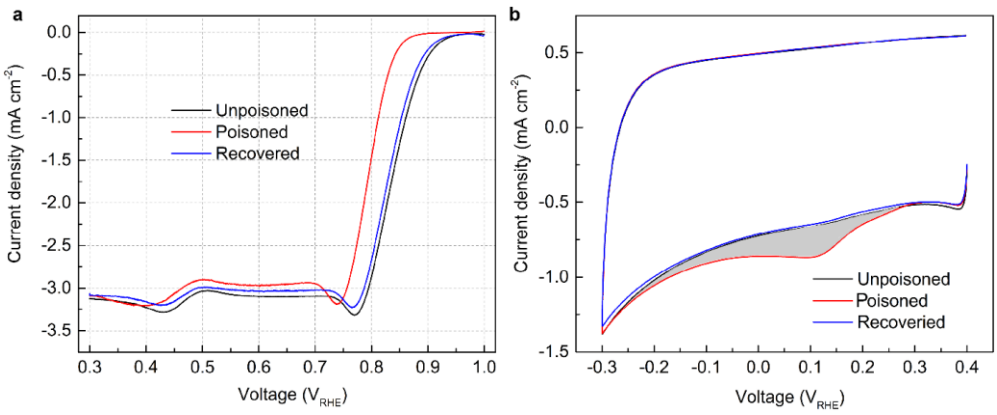

Figure 6. Site density measurement of the Fe-N-C_g catalyst. (a) The linear scan ORR performance without (labeled as 'Unpoisoned'), with NO_2^- poisoning (labeled as 'Poisoned') and after NO_2^- poisoning stripping (labeled as 'Recovered') in oxygen-saturated 0.5 M sodium acetate buffer (pH 5.2) with a 0.27 mg cm^{-2} loading, 10 mV/s of scan rate, and 900 r.p.m. ORR performance is corrected by the CV collected in the Ar-saturated same electrolyte with 10 mV/s of scan rate and without rotation. **(b)** NO_2^- stripping voltammetry in Ar-saturated same electrolyte with 10 mV/s of scan rate and without rotation. The grey area is associated with NO_2^- reductive stripping.

3 Conclusions

In this study, a Fe-N-C catalyst with a porous network structure integrated with high active site density has been constructed with a self-sacrificial template. RDE measurements showed that the Fe-N-C_g catalyst exhibits a high ORR activity with a half-wave potential of 0.85 V and 16 mA cm^{-2} (20 mA per milligram catalyst) of kinetic current density at 0.8 V. The Fe-N-C cathode demonstrated a peak power density of 0.53 W cm^{-2} in an H_2/air PEMFCs owing to its excellent mass transport property. This result suggests that self-sacrificing template synthesis followed by the CVD method for the formation of FeN_4 active sites is promising to independently optimize site densities as well as mass transport.

Experimental section

Synthesis of graphitic carbon nitride (g-C_3N_4). 6 g melamine (Sigma Aldrich) was pyrolyzed at 550 °C for 4 hours in the air in a muffle furnace. The ramping rate was 5 °C/min. The resultant yellow graphitic carbon nitride (g-C_3N_4) was ball milled for 10 minutes with a ball-to-powder mass ratio of 1 in a 35 ml grinding vial polypropylene with an attached flip cap with 3/8" (9.5 mm) methacrylate grinding balls (SPEX SamplePrep, Mixer/Mill 8000M).

Synthesis of zeolitic imidazolate framework-8 /graphitic carbon nitride integrated precursor (ZIF-8/g-C_3N_4). 0.5 g of the ball-milled g-C_3N_4 and 9.852 g of 2-methylimidazole (99%, Sigma-Aldrich) were dispersed into 500 mL pure methanol solution (Sigma-Aldrich) and sonicated for 10 hours. 8.924 g Zn $(NO_3)_2 \cdot 6H_2O$ (≥ 99.0%, Sigma-Aldrich) in 100 mL methanol was added all at once to the above solution under stirring for 1 hour at room temperature. Then let the suspension stand for 4 hours before being collected by centrifuge (IEC Centra-CL2 Centrifuge) with fresh methanol at 3000 rpm for 1 hour and repeated three times, and then dried at 60 °C for 12 hours in a vacuum oven.

Synthesis of Zn-N-C_g substrate. 1.0 g of ZIF-8/g-C_3N_4 integrated precursor and 0.25 g of 1,10 phenanthroline (Sigma-Aldrich) were dispersed in a 50 mL solution of ethanol/water with a volume ratio of 2:1. The mixture was magnetically stirred for 2 hours and dried at 80 °C in a vacuum oven for 12 hours. The dry powders were ball-milled for 30 min in a 35 mL grinding vial with a ball-to-powder mass ratio of 1-to-1. The collected powders were pyrolyzed at 1050 ℃ in argon (a flow rate of 0.65 $L \cdot min^{-1}$)with a ramping rate of 5 °C /min and held at 1050 ℃ for 1 hour, followed by cooling down to room temperature in argon. The powders were collected (denoted as Zn-N-C_g) and were stored in an 80 ℃ vacuum oven before electrochemical testing and/or physicochemical characterization to prevent adsorbing water.

Synthesis of Fe-N-C_g catalyst. The mixture of NH_4Cl (Alfa Aesar) and Fe_2O_3 (Sigma Aldrich) with a mass ratio of 2-to-1 was ball-milled for 5 mins. 120 mg of the mixture was placed in a ceramic boat,

located upstream of the Ar flow in a quartz furnace tube. 80 mg of Zn-N-C_g was uniformly dispersed in a thin layer (8 cm × 4 cm) and positioned downstream with an interval distance of two centimeters away from the mixture of NH_4Cl and Fe_2O_3. The furnace continuously flowed argon with a flow rate of 0.65 $L \cdot min^{-1}$ in the pyrolysis process. The furnace was successively held at 40 ℃ and 100 ℃ for one hour, respectively, to remove water and impurities. Following this the furnace temperature was increased to 750 ℃ with a ramping rate of 25 ℃ min^{-1}, and held at 750 ℃ for 3 hours, followed by cooling down to room temperature. The downstream powders were collected and subjected to magnetic purification by slowly moving a small magnet ~ 0.5 cm above the powder layer to remove Fe nanoparticles. The catalyst was labeled as Fe-N-C_g and stored in a vacuum desiccator before electrochemical testing and physicochemical characterization.

Rotating disk electrode (RDE). A thin-film rotating disk electrode was used to evaluate the ORR activities of the Zn-N-C_g substrate and Fe-N-C_g catalyst. Catalyst inks were prepared by dispersing 10 mg of the catalyst powders in a mixture of Millipore water (36.5 μL, 18.2 MΩ cm) and ethanol (300 μL, Sigma-Aldrich, 99.8%). 5 wt% Nafion solution (108.5 μL, Sigma-Aldrich) was then added into the solution as a binder phase. The resulting mixture was sonicated for 45 minutes in an ice bath (VWR MODEL 50), and then an aliquot of 8.8 μL was drop-cast onto a glassy carbon electrode (0.2463 cm^2, Pine instrument) reaching 800 $\mu g \cdot cm^{-2}$ of catalyst loading. The glassy carbon electrode with the deposited catalyst layer as a working electrode was used in a three-electrode cell set-up connected to a potentiostat (Autolab PGstat 30) and rotator (Pine Instruments). A graphite rod and reversible hydrogen electrode (RHE) were used as counter and reference electrodes, respectively. The ORR activities were measured *via* steady-state RDE polarization curves in O_2-saturated 0.5 M H_2SO_4 (95-97%, Sigma-Aldrich) solutions using a rotation rate of 900 *rpm*, 20-mV potential steps from 0.05 to 0.95 V, and a 25-second potential hold time at each step at room temperature. The cyclic voltammetry (CV) was carried out between 0.05 to 0.95 V *vs.* RHE with a scan rate of 10 $mV \cdot s^{-1}$ in an Ar-saturated 0.5 M H_2SO_4 solution.

Nitrite stripping. A three-electrode cell was used to conduct nitrite stripping. The working electrode was

a 0.2463 cm^2 glassy carbon electrode with 0.27 $mg \cdot cm^{-2}$ loading of Fe-N-C_g catalyst. The counter and reference electrodes were a graphite rod and an Ag/AgCl electrode, respectively. A Pt wire was used to correct the Ag/AgCl scale to the reversible hydrogen electrode (RHE) scale. A 0.5 M acetate buffer (pH 5.2) was prepared with sodium acetate (Sigma-Aldrich) and glacial acetic acid (Sigma-Aldrich). The experimental procedures included protocols for cleaning, poisoning, and recovery of the working electrode, following the previous report by Malko *et al.*.[43, 45] In brief, the working electrode was subjected to potential cycling from 1.05 V to -0.4 V with scan rates of 100 mV/s and 10 mV/s in Ar-saturated electrolyte (20 cycles). It was repeated until stable CVs were obtained. The ORR polarization curves (noted as Unpoisoned) (from 1.0 V to 0.3 V_{RHE}) were collected in O_2-saturated electrolyte using a rotation rate of 900 rpm and a scan rate of 10 $mV \cdot s^{-1}$ followed by the acquisition of a CV in Ar-saturated electrolyte in the same potential range. The latter was used to correct the ORR polarization curves from the point of view of the double-layer capacitance. In addition, the CV curves in the range of 0.4 V to -0.3 V were collected with a scan rate of 10 mV/s. For nitride deposition and subsequent stripping, the working electrode was immersed in 0.125 M $NaNO_2$ solution under rotation at 300 rpm for 5 minutes at open circuit potential (OCP). Subsequently, the working electrode was washed with DI water (1 minute), and electrolyte (5 minutes) with a final rinse in DI water (1 minute) under rotation at 300 rpm. The ORR polarization curves and CV curves of the poisoned electrode (noted as Poisoned) as well as its stripping curves were recorded in sequence with the same parameters used for collecting unpoisoned ORR polarization curves. This step was repeated to verify the recovery of ORR polarization curves and features of CV curves (noted as Recovered).

Polymer electrolyte membrane fuel cell tests.

MEA_{blade_Nafion} and $MEA_{blade\_Aquivion:}$ The Fe-N-C_g catalyst/ionomer slurry was prepared with a solvent-to-ionomer mass ratio of 60. The solvent mixture was prepared with a 1:4 ratio (by mass) of isopropanol and deionized water (18.2 $m\Omega \cdot cm$). After the solvent was added to the catalyst, the mixture was sonicated for 10 min. Then, the required amount of ionomer (Nafion D521 (EW 1100 g/mol) or Aquivion D72-25BS

(EW 720 g/mol)) solution was added to the mixture. The ionomer-to-carbon ratio was 1. The mixture was sonicated for 2 hours in a bath sonicator, and the temperature of the bath was maintained below 30°C. The slurry was blading coated on the Nafion NR211 membrane. 20 wt% Pt/C (TEC10V20E) was used in the anode electrode with an ionomer-to-carbon ratio of 0.5 (20 wt% Nafion solution (D2020)). The EIS measurements were measured at 0.5 A/cm^2 with the same parameters as for polarization curves in H_2/air conditions.

A commercially available fuel cell hardware (Fuel Cell Technologies, Albuquerque, NM, USA) with a custom flowfield was used for each test. Fabricated MEAs were assembled with a 2.5 cm^2 active area using SGL 29BC gas diffusion layers on both the anode and cathode. Fuel cells were tested using a commercial test station (850e, Scribner Associates Inc., Southern Pines, NC). First, the cell was heated to 80°C with 0.5 L/min of N_2 at 100% RH flowing over the anode and cathode for 2 h to hydrate the membrane and ionomer. Polarization curves were measured under differential conditions with 0.5 L/min of H_2 and 2.0 L/min of air on the anode and cathode respectively. Pressure at the anode and cathode was 150 kPa absolute.

MEA_{spray_Nafion}: The slurry of Fe-N-C_g catalyst was dispersed into the mixture of water and 1-propanol aqueous (the volume ratio of water to 1-propanol is 4.5). Nafion D521 dispersion (Ion power, 5.0 wt %) was added with the ionomer-to-carbon ratio of 1. The ink was sonicated for an hour and a half in an ice bath before spray-coating on the H23C6 gas diffusion layer (Freudenberg). A thin Nafion overspray layer with a loading of 0.5 mg cm^{-2} was applied to the surface of the cathode electrode to reduce the contact resistance. The anode Pt electrode (47.7 wt% Pt/C (TKK)) was fabricated by spray coating ink on the SGL 29-BC gas diffusion layer (Sigracet) with an ionomer-to-carbon ratio of 0.85 and a loading of 0.2 mg cm^{-2}. For membrane electrode assembly (MEA), the anode electrode was first hot-pressed onto NR211 membrane (Ion Power) at 145 °C for 4 minutes, and subsequently, the cathode was hot-pressed onto another side of the Nafion film at 145 °C for 3 minutes. The MEA was integrated into a single cell with single-serpentine flow channels at a compression ratio of around 75%. The single cell was then

connected to a fuel cell test station (100 W, Scribner 850e, Scribner Associates). The cells were conditioned under an N_2 environment at 80 °C with 100% relative humidity for 2 hours. Air flowing at 1000 ml·min^{-1} and H_2 (purity 99.999%) flowing at 500 ml·min^{-1} were used for the cathode and anode electrodes, respectively. The total absolute pressure applied to the MEA was 1.5 bar. Fuel cell polarization curves were recorded in a voltage control mode.

Physical characterization

TEM. Transmission electron microscope (TEM) imaging of the ZIF-8/g-C_3N_4 precursor was conducted on a JEOL 2010 field emission gun (FEG).

STEM-EDS. EDS elemental maps were recorded at STEM mode with Thermo-Fisher Talos F200X at an accelerating voltage of 200 kV. Fe L and N K edges elemental maps were extracted, and overlaying maps were generated. High-angle annular dark-field (HAADF) STEM images were collected using a Hitachi HD2700C with the Cs probe corrector operated at 200 kV.

SEM. Scanning electron microscopy (SEM) micrographs of the Fe-N-C_g catalyst and Zn-N-C_g substrate were obtained with a Hitachi S-4800 apparatus (Hitachi, Tokyo, Japan).

XRD. X-ray diffraction (XRD) patterns were collected by using a PANanalytical X'Pert Pro powder X-ray diffractometer with Cu K_α radiation.

N_2 adsorption/desorption analysis. Surface areas were measured by the Brunauer-Emmett-Teller (BET) method using N_2 adsorption/desorption on an Autosorb-1 analyzer (Quantachrome Instruments). N_2 sorption analysis was conducted at liquid nitrogen temperature (77K). Before the measurements, the Fe-N-C_g catalyst and Zn-N-C_g substrates power were degassed at 200 °C for 2 hours in flowing nitrogen to remove moisture. The pore size distribution was calculated by the density functional theory (DFT) model.

XAS measurements. The *ex situ* XAS spectra at the Zn K-edge for the Zn-N-C_g substrate and Fe K-edge

for the Fe-N-C_g catalysts were collected in transmission mode at the beamline 7-BM of National Synchrotron Light Source II (NSLS-II) of Brookhaven National Laboratory. The XAS data were processed and fitted using the Ifeffit−based Athena and Artemis programs.[46] Scans were calibrated, aligned, and normalized with the background removed using the IFEFFIT suite.[47] The χ(R) were modeled using single scattering paths calculated by FEFF6.[48]

Acknowledgments

The US Department of Energy supported this work under award numbers DE-EE0008416 ~~and DE-EE0008075~~ and the Northeastern University Dissertation Completion Fellowship. The *ex situ* XAS experiments were performed at the beamlines 7-BM of the National Synchrotron Light Source II, a U.S. Department of Energy (DOE) Office of Science User Facility operated for the DOE Office of Science by Brookhaven National Laboratory. This research used the Center for Functional Nanomaterials, a U.S. DOE Office of Science Facility, at Brookhaven National Laboratory. G.L. acknowledges the support of the US National Science Foundation through Award 2102655 (N_2 adsorption/desorption analysis)

CONFLICT OF INTEREST

The authors declare no conflict of interest.

REFERENCES

[1] Debe, M. K. Electrocatalyst approaches and challenges for automotive fuel cells, *Nature* **2012,** 486 (7401), 43-51.
[2] Zitolo, A.; Goellner, V.; Armel, V.; Sougrati, M. T.; Mineva, T.; Stievano, L.; Fonda, E.; Jaouen, F. Identification of catalytic sites for oxygen reduction in iron- and nitrogen-doped graphene materials, *Nat Mater* **2015,** 14 (9), 937-42.
[3] Jia, Q.; Ramaswamy, N.; Hafiz, H.; Tylus, U.; Strickland, K.; Wu, G.; Barbiellini, B.; Bansil, A.; Holby, E. F.; Zelenay, P.; Mukerjee, S. Experimental Observation of Redox-Induced Fe-N Switching Behavior as a Determinant Role for Oxygen Reduction Activity, *ACS Nano* **2015,** 9 (12), 12496-505.
[4] Li, J.; Jiao, L.; Wegener, E.; Richard, L. L.; Liu, E.; Zitolo, A.; Sougrati, M. T.; Mukerjee, S.; Zhao, Z.; Huang, Y.; Yang, F.; Zhong, S.; Xu, H.; Kropf, A. J.; Jaouen, F.; Myers, D. J.; Jia, Q. Evolution Pathway from Iron Compounds to Fe1(II)-N4 Sites through Gas-Phase Iron during Pyrolysis, *J Am Chem Soc* **2020,** 142 (3), 1417-1423.
[5] Mehmood, A.; Gong, M.; Jaouen, F.; Roy, A.; Zitolo, A.; Khan, A.; Sougrati, M.-T.; Primbs, M.; Bonastre, A. M.; Fongalland, D.; Drazic, G.; Strasser, P.; Kucernak, A. High loading of single atomic iron sites in Fe–NC oxygen reduction catalysts for proton exchange membrane fuel cells, *Nature Catalysis* **2022,** 5 (4), 311-323.

[6] Jiao, L.; Li, J.; Richard, L. L.; Sun, Q.; Stracensky, T.; Liu, E.; Sougrati, M. T.; Zhao, Z.; Yang, F.; Zhong, S.; Xu, H.; Mukerjee, S.; Huang, Y.; Cullen, D. A.; Park, J. H.; Ferrandon, M.; Myers, D. J.; Jaouen, F.; Jia, Q. Chemical vapour deposition of Fe-N-C oxygen reduction catalysts with full utilization of dense Fe-N4 sites, *Nat. Mater.* **2021,** 20 (10), 1385-1391.
[7] Hoon T. Chung; David A. Cullen; Drew Higgins; Brian T. Sneed; Edward F. Holby; Karren L. More; Zelenay, P. Direct atomic-level insight into the active sites of a high-performance PGM-free ORR catalyst, *Science* **2017,** 357, 479-484.
[8] Asad Mehmood; Mengjun Gong; Frédéric Jaouen; Aaron Roy; Andrea Zitolo; Anastassiya Khan; Moulay-Tahar Sougrati; Mathias Primbs; Alex Martinez Bonastre; Dash Fongalland; Goran Drazic; Peter Strasser; Kucernak, A. High loading of single atomic iron sites in Fe-NC oxygen reduction catalysts for proton exchange membrane fuel cells, *Nature Catalysis* **2022,** 5, 311-323.
[9] Michel Lefèvre; Eric Proietti; Frédéric Jaouen; Dodelet, J.-P. Iron-Based Catalysts with Improved Oxygen Reduction Activity in Polymer Electrolyte Fuel Cells, *Science* **2009,** 324, 71-74.
[10] Osmieri, L.; Wang, H.; Neyerlin, K. C. Impact of Fabrication and Testing Parameters on the Performance of a Polymer Electrolyte Fuel Cell with Platinum Group Metal (PGM)-Free Cathode Catalyst, *Journal of The Electrochemical Society* **2021,** 168 (1).
[11] Qiao, M.; Wang, Y.; Wang, Q.; Hu, G.; Mamat, X.; Zhang, S.; Wang, S. Hierarchically Ordered Porous Carbon with Atomically Dispersed FeN4 for Ultraefficient Oxygen Reduction Reaction in Proton-Exchange Membrane Fuel Cells, *Angew Chem Int Ed Engl* **2020,** 59 (7), 2688-2694.
[12] Zhang, H.; Xia, W.; Ge, J.; Tang, J. Hierarchically ordered macro-microporous metal-organic framework derived oxygen reduction electrocatalyst, *Chemical Engineering Journal* **2022,** 429.
[13] Pampel, J.; Fellinger, T.-P. Opening of Bottleneck Pores for the Improvement of Nitrogen Doped Carbon Electrocatalysts, *Advanced Energy Materials* **2016,** 6 (8).
[14] Han, J.; Bao, H.; Wang, J.-Q.; Zheng, L.; Sun, S.; Wang, Z. L.; Sun, C. 3D N-doped ordered mesoporous carbon supported single-atom Fe-N-C catalysts with superior performance for oxygen reduction reaction and zinc-air battery, *Applied Catalysis B: Environmental* **2021,** 280.
[15] Yang, X.; Wang, Y.; Zhang, G.; Du, L.; Yang, L.; Markiewicz, M.; Choi, J.-y.; Chenitz, R.; Sun, S. SiO2-Fe/N/C catalyst with enhanced mass transport in PEM fuel cells, *Applied Catalysis B: Environmental* **2020,** 264.
[16] Xin Wan; Xiaofang Liu; Yongcheng Li; Ronghai Yu; Lirong Zheng; Wensheng Yan, H. W.; Ming Xu4; Shui, J. Fe–N–C electrocatalyst with dense active sites
and efficient mass transport for high-performance
proton exchange membrane fuel cells, *Nature Catalysis* **2019,** 2, 259-268.
[17] Shi, L.; Lin, X.; Liu, F.; Long, Y.; Cheng, R.; Tan, C.; Yang, L.; Hu, C.; Zhao, S.; Liu, D. Geometrically Deformed Iron-Based Single-Atom Catalysts for High-Performance Acidic Proton Exchange Membrane Fuel Cells, *ACS Catalysis* **2022,** 12 (9), 5397-5406.
[18] Chen, G.; Liu, P.; Liao, Z.; Sun, F.; He, Y.; Zhong, H.; Zhang, T.; Zschech, E.; Chen, M.; Wu, G.; Zhang, J.; Feng, X. Zinc-Mediated Template Synthesis of Fe-N-C Electrocatalysts with Densely Accessible Fe-Nx Active Sites for Efficient Oxygen Reduction, *Adv. Mater.* **2020,** 32 (8), e1907399.
[19] Zhu, C.; Shi, Q.; Xu, B. Z.; Fu, S.; Wan, G.; Yang, C.; Yao, S.; Song, J.; Zhou, H.; Du, D.; Beckman, S. P.; Su, D.; Lin, Y. Hierarchically Porous M‐N‐C (M = Co and Fe) Single‐Atom Electrocatalysts with Robust MN_x Active Moieties Enable Enhanced ORR Performance, *Adv. Energy Mater.* **2018,** 8 (29).
[20] Hoon T. Chung; David A. Cullen; Drew Higgins; Brian T. Sneed; Edward F. Holby; Karren L. More; Zelenay, P. Direct atomic-level insight into the active sites ofa high-performance PGM-free ORR catalyst, *Science* **2017,** 357, 479–484.
[21] Jia, Q.; Ramaswamy, N.; Tylus, U.; Strickland, K.; Li, J.; Serov, A.; Artyushkova, K.; Atanassov, P.; Anibal, J.; Gumeci, C.; Barton, S. C.; Sougrati, M.-T.; Jaouen, F.; Halevi, B.; Mukerjee, S. Spectroscopic insights into the nature of active sites in iron–nitrogen–carbon electrocatalysts for oxygen reduction in acid, *Nano Energy* **2016,** 29, 65-82.
[22] Schneider, P. Adsorption isotherms of microporous-mesoporous solids revisited, *Applied Catalysis A: General* **1995,** 129, 157-165.
[23] Sebastian storch; helmut bretinger; Maier, W. F. Characterization of micro- and mesoporous solids by physisorption methods and pore-size analysis, *Applied Catalysis A: General* **1998,** 174, 137-146.
[24] Deng, Y.; Chi, B.; Tian, X.; Cui, Z.; Liu, E.; Jia, Q.; Fan, W.; Wang, G.; Dang, D.; Li, M.; Zang, K.; Luo, J.; Hu, Y.; Liao, S.; Sun, X.; Mukerjee, S. g-C_3N_4 Promoted MOF Derived Hollow Carbon Nanopolyhedra Doped with High Density/fraction of Single Fe Atoms as an Ultra-high Performance Non-precious Catalyst towards Acidic ORR

and PEM Fuel Cells, *J. Mater. Chem. A* **2019,** 7 (9), 5020-5030.
[25] Osmieri, L.; Park, J.; Cullen, D. A.; Zelenay, P.; Myers, D. J.; Neyerlin, K. C. Status and challenges for the application of platinum group metal-free catalysts in proton-exchange membrane fuel cells, *Current Opinion in Electrochemistry* **2021,** 25.
[26] Primbs, M.; Sun, Y.; Roy, A.; Malko, D.; Mehmood, A.; Sougrati, M.-T.; Blanchard, P.-Y.; Granozzi, G.; Kosmala, T.; Daniel, G.; Atanassov, P.; Sharman, J.; Durante, C.; Kucernak, A.; Jones, D.; Jaouen, F.; Strasser, P. Establishing reactivity descriptors for platinum group metal (PGM)-free Fe–N–C catalysts for PEM fuel cells, *Energy & Environmental Science* **2020,** 13 (8), 2480-2500.
[27] Wang, G.; Osmieri, L.; Star, A. G.; Pfeilsticker, J.; Neyerlin, K. C. Elucidating the Role of Ionomer in the Performance of Platinum Group Metal-free Catalyst Layer via in situ Electrochemical Diagnostics, *Journal of The Electrochemical Society* **2020,** 167 (4).
[28] Xin, L.; Yang, F.; Xie, J.; Yang, Z.; Kariuki, N. N.; Myers, D. J.; Peng, J.-K.; Wang, X.; Ahluwalia, R. K.; Yu, K.; Ferreira, P. J.; Bonastre, A. M.; Fongalland, D.; Sharman, J. Enhanced MEA Performance for PEMFCs under Low Relative Humidity and Low Oxygen Content Conditions via Catalyst Functionalization, *Journal of The Electrochemical Society* **2017,** 164 (6), F674-F684.
[29] K. C. Neyerlin; Hubert A. Gasteiger; Cortney K. Mittelsteadt; Jacob Jorne; Gu, W. Effect of Relative Humidity on Oxygen Reduction Kinetics in a PEMFC, *J. Electrochem. Soc.* **2005,** 152 (6), A1073-A1080.
[30] Zhang, J.; Tang, Y.; Song, C.; Xia, Z.; Li, H.; Wang, H.; Zhang, J. PEM fuel cell relative humidity (RH) and its effect on performance at high temperatures, *Electrochimica Acta* **2008,** 53 (16), 5315-5321.
[31] Liu, Y.; Ji, C.; Gu, W.; Jorne, J.; Gasteiger, H. A. Effects of Catalyst Carbon Support on Proton Conduction and Cathode Performance in PEM Fuel Cells, *Journal of The Electrochemical Society* **2011,** 158 (6), B614-B621.
[32] Shinozaki, K.; Yamada, H.; Morimoto, Y. Relative Humidity Dependence of Pt Utilization in Polymer Electrolyte Fuel Cell Electrodes: Effects of Electrode Thickness, Ionomer-to-Carbon Ratio, Ionomer Equivalent Weight, and Carbon Support, *Journal of The Electrochemical Society* **2011,** 158 (5).
[33] S. P. Wasik; Mcculloh, K. E. Measurements of Gaseous Diffusion Coefficients by a Gas Chromatographic Technique, *Journal of Research of the National Bureau of Standards-A. Physics and Chemistry* **1969,** 73A, 207-211.
[34] Cruz-Manzo, S.; Greenwood, P. Study of oxygen diffusion in the cathode catalyst layer and gas diffusion layer for polymer electrolyte fuel cells with EIS, *Journal of Electroanalytical Chemistry* **2021,** 892.
[35] ChungHyuk Lee; Wilton J. M. Kort-Kamp; Haoran Yu; David A. Cullen; Brian M. Patterson; Tanvir Alam Arman; Siddharth Komini Babu; Rangachary Mukundan; Rod L. Borup; Spendelow, J. S. Grooved electrodes for high-power-density fuel cells, *Nature Energy* **2023,** 8, 685-694.
[36] Gerling, C.; Hanauer, M.; Berner, U.; Andreas Friedrich, K. PEM Single Cells under Differential Conditions: Full Factorial Parameterization of the ORR and HOR Kinetics and Loss Analysis, *Journal of The Electrochemical Society* **2022,** 169 (1).
[37] E. Bradley Easton; Toby D. Astill; Holdcroft, S. Properties of Gas Diffusion Electrodes Containing Sulfonated Poly(ether ether ketone), *J. Electrochem. Soc.* **2005,** 152, A752-A758.
[38] Hui Xu; Kunz, , H. R.; Leonard J. Bonville; Fenton, J. M. Improving PEMFC Performance Using Low Equivalent Weight PFSA Ionomers and Pt-Co/C Catalyst in the Cathode, *J. Electrochem. Soc.* **2007,** 152, B271-B278.
[39] Jinnouchi, R.; Kudo, K.; Kodama, K.; Kitano, N.; Suzuki, T.; Minami, S.; Shinozaki, K.; Hasegawa, N.; Shinohara, A. The role of oxygen-permeable ionomer for polymer electrolyte fuel cells, *Nat Commun* **2021,** 12 (1), 4956.
[40] Shimizu, R.; Park, Y.-C.; Kakinuma, K.; Iiyama, A.; Uchida, M. Effects of Both Oxygen Permeability and Ion Exchange Capacity for Cathode Ionomers on the Performance and Durability of Polymer Electrolyte Fuel Cells, *Journal of The Electrochemical Society* **2018,** 165 (6), F3063-F3071.
[41] Wang, X.; Ferrandon, M.; Park, J. H.; Shen, J.-J.; Kropf, A. J.; Zhang, H.; Zelenay, P.; Myers, D. J. Iron redox behavior and oxygen reduction activity of Fe-N-C electrocatalysts in different electrolytes, *Electrochimica Acta* **2023,** 443.
[42] Malko, D.; Kucernak, A.; Lopes, T. In situ Electrochemical Quantification of Active Sites in Fe-N/C Non-precious Metal Catalysts, *Nat. Commun.* **2016,** 7, 13285.
[43] Malko, D.; Kucernak, A.; Lopes, T. Performance of Fe-N/C Oxygen Reduction Electrocatalysts toward NO2(-), NO, and NH2OH Electroreduction: From Fundamental Insights into the Active Center to a New Method for Environmental Nitrite Destruction, *J Am Chem Soc* **2016,** 138 (49), 16056-16068.
[44] Kim, D. H.; Ringe, S.; Kim, H.; Kim, S.; Kim, B.; Bae, G.; Oh, H. S.; Jaouen, F.; Kim, W.; Kim, H.; Choi, C. H.

Selective electrochemical reduction of nitric oxide to hydroxylamine by atomically dispersed iron catalyst, *Nat Commun* **2021,** 12 (1), 1856.
[45] Malko, D.; Kucernak, A.; Lopes, T. In situ Electrochemical Quantification of Active Sites in Fe–N/C Non-precious Metal Catalysts, *Nat. Commun.* **2016,** 7 (1), 13285.
[46] Ravel, B.; Newville, M. ATHENA, ARTEMIS, HEPHAESTUS: data analysis for X-ray absorption spectroscopy using IFEFFIT, *J Synchrotron Radiat* **2005,** 12 (Pt 4), 537-41.
[47] Newville, M. IFEFFIT: interactive XAFS annalysis and FEFF fitting, *J. Synchrotron Rad.* **2001,** 8, 322-324.
[48] A. L. Ankudinov; B. Ravel; J. J. Rehr; Conradson, S. D. Real-space multiple-scattering calculation and interpretation of x-ray-absorption near-edge structure, *Physical Review B* **1998,** 58 (12), 7565-7576.